Catalysis Communications 175 (2023) 106605

Contents lists available at ScienceDirect

Catalysis Communications

journal homepage: www.elsevier.com/locate/catcom

Development of highly active and coke-resilient Ni-based catalysts for low-temperature steam reformation of methane

Sardar Ali *, Ahmed Gamal, Mahmoud M. Khader

Gas Processing Center, College of Engineering, Qatar University, 2713 Doha, Qatar

ARTICLE INFO

Keywords:
Ni nanoparticles
$NiAl_2O_4$ nanocrystallites
Solution combustion synthesis
Low temperature methane steam reforming

ABSTRACT

In this work, we report on the development of highly active and stable catalysts for low temperature steam reformation of methane. The Ni-based catalysts supported on alumina were synthesized by the single step solution combustion synthesis (SCS) method. A combination of various surface and bulk sensitive analytical techniques such as XRD, cyclic TPDRO, XPS and HRTEM-SAED was utilized for detailed characterization of the catalysts. The catalyst 5NC synthesized by the SCS method exhibited superior activity and excellent stability for steam reformation of methane during the investigated period on stream for around 200 h. The light-off for methane conversion over the 5NC catalyst started at a reaction temperature of 350 °C whereas for the 5NP catalyst no activity below 600 °C was observed. Moreover, full methane conversion over the 5NC catalyst was achieved at 700 °C. Under similar conditions at reaction temperature of 700 °C, the methane decomposition rates over the 5NC catalyst was around 20 times higher than that of the 5NP catalyst. The exceptional high performance of the 5NC catalyst was attributed to the presence of surface defects, generation of nickel aluminates ($NiAl_2O_4$) nano-crystallites, uniform distribution and smaller metal oxide particle size.

1. Introduction

Steam reformation of methane (SRM) deals with the thermocatalytic conversion of natural gas into syngas (CO + H_2) and/or hydrogen (H_2) [1,2]. These products are valuable feedstock for various value added petrochemicals. Due to high heating value of around 140 kJ/g and carbon free nature hydrogen, especially, seems to be an attractive alternative energy source and hence making SRM process an important starting process in emerging hydrogen economy [3,4]. The steam reformation consists of three reversible reactions shown in Eq. (1), Eq. (2) and Eq. (3), respectively [5,6]. Two of the endothermic whereas the water gas shift reaction is exothermic in nature [7].

$$CH_4 + H_2O \rightleftharpoons CO + 3H_2 \ \Delta H = +206 \text{ kJ/mol} \quad (1)$$

$$CO + H_2O \rightleftharpoons CO_2 + H_2 \ \Delta H = -41 \text{ kJ/mol} \quad (2)$$

$$CH_4 + 2H_2O \rightleftharpoons CO_2 + 4H_2 \ \Delta H = +165 \text{ kJ/mol} \quad (3)$$

The effluents of the SRM process consist of CO, H_2, CO_2, steam and unreacted CH_4 and the overall products distribution is governed by various factors such as type of the reactor, feed composition, nature of the catalysts and operation temperature [8,9]. Various transitions metals belonging to group VIII-X such as nickel, cobalt, ruthenium, rhodium, palladium and platinum have been reported to exhibit considerable activity for this process [9–12]. For large-scale industrial applications due to better activity, cost effectiveness and availability, Ni-based catalysts are preferred choices [13–15]. However, deactivation of the Ni-based catalysts due to phase transformation of active nickel sites, coke deposition and operation at higher temperature of >800 °C are the key main challenges in designing efficient catalysts for the SRM [16–18]. Particularly, in the commercial plants, coke deposition may results serious issues such as increase the mass and heat transfer resistance, break up the catalyst pellets, the pressure drop, and masking of the Ni active sites [5]. In the stream reformation reaction carbon formation can take place due to the Boudouard reaction (CO disproportionation) and/or methane cracking [19,20]. Both of these reactions are represented in Eq. (4) and Eq. (5), respectively.

$$2CO \rightleftharpoons C + CO_2 \ \Delta H = -172 \text{ kJ/mol} \quad (4)$$

$$CH_4 \rightleftharpoons C + 2H_2 \ \Delta H = +74.87 \text{ kJ/mol} \quad (5)$$

Therefore, for an efficient SRM process development of active and stable Ni-based catalysts are highly desirable. It is generally accepted

* Corresponding author at: Gas Processing Center, Building H10 new research complex, Zone F, Office F111, Qatar University, P.O. Box 2713, Doha, Qatar.
E-mail address: ali.sardar@qu.edu.qa (S. Ali).

https://doi.org/10.1016/j.catcom.2023.106605
Received 17 November 2022; Received in revised form 29 December 2022; Accepted 11 January 2023
Available online 13 January 2023

that the metal support interaction play a crucial role in activity and stability of the Ni-based catalysts for SRM [21]. Therefore, with the major concern of aiming to synthesize highly efficient Ni-based methane reformation catalysts, metal oxides such as (ZrO_2) zirconia and ceria (CeO_2) have been researched as supports and were believed to assist oxidation of the coke deposited on the catalyst surface [22]. However, high oxygen mobility of these support were reported to result in phase transformation of metallic nickel (Ni^o) to nickel oxides (NiO) and consequently resulted in considerable loss in the activity. Even though, incorporation of various precious metals have reported to result in coke resilience of the catalysts, however high cost of these metals limits the commercial applicability [23]. Alloying nickel with several other metals such as tin (Sn), manganese (Mn), magnesium (Mg), molybdenum (Mo) and copper (Cu) were also reported to suppress coke formation, however a considerable loss in the activity due to coverage of the active sites were recorded [24].

For the development of highly efficient RSM catalysts, induced nickel and alumina phase in the form of nickel aluminate ($NiAl_2O_4$) spinels and/or nanocrystallites have also been reported to result in improved activity of the Ni-based catalysts. High catalytic performance of these catalysts have been attributed to the presence of surface defects and reducible nickel species at the interference of $NiAl_2O_4$ spinels structures [25–28]. For example, Salhi and co-workers synthesized $NiAl_2O_4$ catalysts using pseudo gel method. These catalysts were reported to possess high activity for steam reformation reaction that was attributed to the presence of oxygen vacancies and surface defects resulting in high activity and stability in the steam reformation reaction [25]. Indeed, there is a large number of number of research reports related to the synthesis of $NiAl_2O_4$ spinels for application to steam reformation of methane. However, the role of nickel aluminates spinels catalysts is still debatable and continuously argued in literature. This is because some of the literature suggest deactivation of Ni/Al_2O_3 catalysts was due to the formation of nickel aluminate structure resulting in masking the active sites and therefore lower activity. Moreover, reducibility of the $NiAl_2O_4$ catalysts seems to be additional challenge for the development of highly active catalysts. Moreover, so far the development of pure and/stoichiometric $NiAl_2O_4$ nanocrystallites is complicated [28–30]. Some recent reported research suggest the importance of the preparation methodology for the preparation of highly efficient $NiAl_2O_4$ catalysts [27]. Our group also previously reported synthesis of Ni-based based catalysts synthesized via solution combustion synthesis (SCS) method were superior in activity and stability than the conventional catalysts during dry reformation of methane. The higher catalytic performance was attributed to the presence of $NiAl_2O_4$ nanocrystallites [31].

It is clear from the above discussion that the development of efficient Ni-based catalysts for steam reformation of methane remains a key challenge for researchers. Therefore, in the present work, we aimed our catalyst development methodology to synthesize highly active, stable and coke resilient Ni-based catalysts for the low temperature steam reformation of methane. This was achieved by utilizing the preparative methodology of solution combustion synthesis. This move was based on attempting to maximize the induction of the nanoparticles of nickel into the alumina matrix resulting in the formation of nanocrystallites of spinel $NiAl_2O_4$. The present study covers synthesis, characterization and catalytic evaluation of the SCS catalysts for steam reformation of methane, in general, and synthesis gas production in particular is presented. For benchmarking, a Ni-based catalyst was also prepared by the conventional co-precipitation method. The composition of both the catalysts were similar.

2. Materials and method

2.1. Catalyst synthesis

The preparative methodology of solution combustion synthesis (SCS) was used to prepare the catalyst with a nickel loading of 5 wt%Ni and supported on alumina. This nickel-based catalyst was denoted as 5NC. Briefly, in the SCS procedure required amounts of the nitrate precursor salts of nickel (nickel (II) nitrate hexahydrate ($Ni(NO_3)_2.6H_2O$, BDH), and alumina (aluminum nitrate hexahydrate ($Al(NO_3)_3{\cdot}9H_2O$, Sigma Aldrich, 99.9%) were dissolved in 50 mL of deionized water in a 500 mL capacity beaker. This mixture was stirred for one hour to get a homogeneous solution. The required amount of glycine (Sigma Aldrich, 98.5%) corresponding to a glycine to oxidant ratio of 0.55 was also added with continuous stirring. This step was followed by slowly heating the resulting solution over a hot plate for combustion. The mixture turned into a viscous jelly after which combustion initiated in a self-sustained manner. At this point heater of hot plate was turned off. The resultant powder was thoroughly mixed followed by calcination at 800 °C with a dwell time of five hours in a muffle furnace with heating rate and cooling rate of +1 °C/min and − 1 °C/min, respectively. The catalytic performance of the 5NC nanocatalyst was benchmarked with that of 5NP catalyst synthesized via co-precipitation method reported in literature [32]. The resultant powder was then dried at 150 °C followed by calcination at aforementioned conditions. In the two cases, 5NC and 5NP, the composition of the catalyst was similar with a nickel content of 5 wt%.

2.2. Catalyst characterization

The analytical technique of room temperature X-ray diffraction (XRD) analysis was employed to study textural properties of the calcined catalysts. The XRD measurements were carried out on a desktop X-ray diffractometer (Rigaku, MiniFlexII). This machine is equipped with a CuK_α radiation source. The analysis was performed at 30 kV and 15 mA, in the scanning angle (2θ) range of 5–80°. Specimen was prepared by packing around 100 mg sample powder in a glass holder. Morphology of the catalysts in terms of metal oxide particle size and particle size distribution was studied by high angle annular dark field (HAADF) high-resolution transmission electron microscopy (HRTEM) equipped with energy dispersive spectroscopy (EDS) using a JEOL 2010 F microscope operated at voltage of 200 kV. For analysis, samples were prepared by dispersing the powder into n-propane by sonication. A small drop of the well dispersed sample was then placed onto a holey carbon film coated copper grid with 200-mesh. HAADF images were recorded with a 0.7 nm HR probe having a collection angle of 54.9 mrad. The N_2 adsorption–desorption analysis was performed using ASAP2020, Micrometrics. Typically, in this procedure, around 0.2 g of the calcined powder was placed in the pre-weighed quartz tube and degassed overnight under the flow of pure helium (He) at 200 °C. The pre-treatment was followed by determining the specific surface area by the BET method using nitrogen gas as adsorbate. Surface chemical composition of the catalysts was studied by a state-of-the-art photoelectron spectrometer (AXIS Ultra DLD, KRATOS). For analysis, around 30 mg of the powder sample was loaded in a bronze stub and introduced into the sample analysis chamber (SAC). Prior to analysis surface of the samples were cleaned by itching with argon ion gun operating at an accelerating voltage of 4KeV. Pressure in the analytical chamber during spectral acquisition was less than 1.0×10^{-9} Torr. High-resolution scans were recorded at pass energy of 20 eV using 10 kV accelerating voltage for monochromatized AlKα source. The sequential reduction following by oxidation and second reduction of the catalysts was investigated by cyclic TPR-TPO using ChemiSorb2750 (Micromeritics) equipped with a thermal conductivity detector (TCD). The first temperature programmed reduction cycle was denoted as H_2-TPR1. This process consisted of two steps namely degassing followed by analysis. For degassing, around 50 mg of sample was loaded into a U-shaped quartz tube followed by raising the reactor temperature to 180 °C at a heating rate of 5 °C min^{-1} in 30 mL min^{-1} of pure argon (Ar). The sample was pretreated at this temperature overnight. The furnace temperature was then cooled down to 30 °C in flowing Ar. The H_2-TPR, was then performed by switching flow to 30 SCCM of 5vol%H_2/Ar and heating from 30 °C to 900 °C at a rate of

5°Cmin^{-1}. The effluent gases were directly passed to the TCD. Once the temperature reached to 900 °C the flow was switched to 30SCCM of pure Ar and the reactor temperature was cooled down to 30 °C at a cooling rate of 5 °C/min. TPR1 was followed by temperature-programmed oxidation (TPO) which was carried out by switching the flow to 30 SCCM of 5 vol%O_2/Ar and raising the temperature from 30 °C to 900 °C at a heating rate of 5 °C/min. The flow was then again switched to 30SCCM of pure Ar and the reactor temperature was cooled down to 30 °C at a cooling rate of 5 °C/min. The second reduction cycle denoted as TPR2 was then recorded following similar conditions used for TPR1. Temperature programmed oxidation (TPO) analyses of the spent catalysts followed by 200 h of time on stream (T.O·S.) during steam reformation reaction at 700 °C was carried out to study nature of the carbon species deposited on the catalysts surface. In this procedure after T.O·S at 700 °C the catalysts were passivated by switching reactant flow to 50mLmin^{-1} of He and decreasing the temperature to 30 °C. TPO analysis was performed loading around 100 mg of the passivated spent catalyst in the tubular quartz reactor connected online to a quadrupole mass spectrometer (Hiden, HPR20). The TPO was recorded by heating the sample from room temperature to 900 °C at a heating ramp of 2°Cmin^{-1} in presence of 20 ml/min of 5%volO_2/Ar.

2.3. Catalytic performance

Catalysts were tested for steam reformation of methane using a fixed bed plug flow quartz reactor. The reactor can be online connected either with GC-TCD (Agilent 2860) or online Quadrupole mass spectrum (Hiden Analytical). For catalytic run around 0.5 cc of the calcined catalyst was sieved in a mesh size of 150 μm to 300 μm and physically mixed with 1.5 cc of quartz powder sieved with similar mesh size was sandwiched in the middle of the reactor using quartz wool. The SRM reaction was performed at atmospheric pressure with a CH_4/steam ratio of three, with a gas hourly space velocity (GHSV) of 9000 h^{-1} and in the temperature range of 350 °C to 900 °C, whereas the stability test was performed at CH_4/steam ratio of unity. Prior to reaction, catalysts were activated by reducing in 30 cc/min of pure hydrogen at 800 °C with a heating increment of +1°Cmin^{-1} for two hours. The temperature was then cooled down to the desirable set point at –1°Cmin^{-1}. Required amount of the 10%CH_4/Ar and steam were introduced into the premixing chamber preheated at 120 °C. Flow of the gases are controlled via precision mass flow controllers whereas water was delivered using HPLC liquid delivery pump assembly (LC-20 CE, Schimadzu). The effluent gases were cold trapped at 5 °C before entering into the online GC or MS analyzer. The percentage of methane conversion and products selectivity were measured using the following equations;

$$\text{Methane Conversion} : CH_4\ \text{Conv.}(\%) = \left[\frac{nCH_4(in) - nCH_4(out)}{nCH_4(in)}\right] x\ 100 \quad (6)$$

$$\text{Carbon Monoxide Selectivity} : CO\ \text{Selec.}(\%) = \left[\frac{nCO(out)}{nCH_4(in) - nCH_4(out)}\right] x\ 100 \quad (7)$$

$$\text{Carbon Dioxide Selectivity} : CO_2\ \text{Selec.}(\%) = \left[\frac{nCO_2(out)}{nCH_4(in) - nCH_4(out)}\right] x\ 100 \quad (8)$$

$$\text{Hydrogen Selectivity} : H_2\ \text{Selec.}(\%) = \left[\frac{nH_2(out)}{nCH4\ (in)}\right] x\ 100 \quad (9)$$

$$\frac{H2}{CO}\ \text{ratio} = \left[\frac{nH_2}{nCO}\right] x\ 100 \quad (10)$$

3. Results and discussions

3.1. Textural properties of the catalysts

The analytical technique of N_2-adsorption and desorption was utilized to study BET surface area and pore structure of the catalysts. The N_2 adsorption and desorption isotherms of the calcined samples are displayed in Fig. 1 and the results are summarized in Table 2. As can be seen in Fig. 1, both the 5NC and 5NP catalysts exhibited type IV isotherm with H3 type of hysteresis loop at higher relative pressure indicating mesoporous nature of the catalysts [33]. The 5NC catalyst exhibited comparatively larger surface area and pore volume than the 5NP catalyst. The surface area for the 5NC and 5NP catalysts was 98.9 m^2/g and 53.6 m^2/g, respectively. Whereas the pore volume for the 5NC and 5NP catalysts was 0.21 cm^3/g and 0.14 cm^3/g, respectively. This behavior can be attributed to the special characteristic of the preparative methodology of the SCS method that proceeds with a significant evolution of gases and thus resulted in creating high porosity and larger surface area than the 5NP catalyst prepared by co-precipitation method.

XRD patterns of the catalysts are displayed in Fig. 2. For the Al_2O_3 support without metal incorporation the diffraction lines at 2θ values of 36.9°, 44.9°, and 65.8°, were attributed to the presence of various phases of alumina [34]. Diffraction patterns of the 5NP catalyst were quite similar to that of the alumina and no distinguishable changes were identified, indicating the presence of well-dispersed particles with smaller size. Contrary to the 5NP catalyst, the 5NC catalyst revealed the presence of new phases at 2θ values of 19.9° that was attributed to the presence of nickel aluminate nanocrystallites [31,35]. Absence of this peak for the conventional catalyst suggest that the preparative methodology of SCS method resulted in the formation of induced nickel alumina phases.

3.2. Ni species distribution in the catalysts

The effect of synthesis method on the nature, distribution and stability of various nickel species was investigated through a combination of surface sensitive and bulk sensitive analytical techniques of HRTEM, XPS, and sequential TPR/ TPO/TPR.

3.2.1. HRTEM analysis

Morphology of the calcined samples in terms of nickel oxide particle size and particle size distribution as well as structure of nickel was

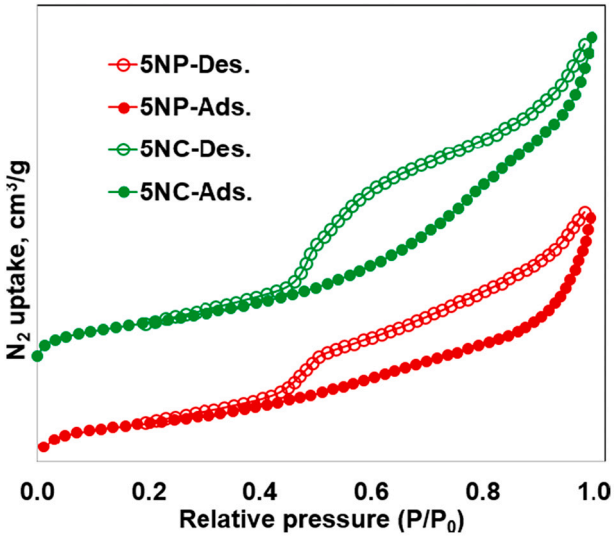

Fig. 1. The N_2 adsorption and desorption isotherms of the calcined 5NP and 5NC catalysts.

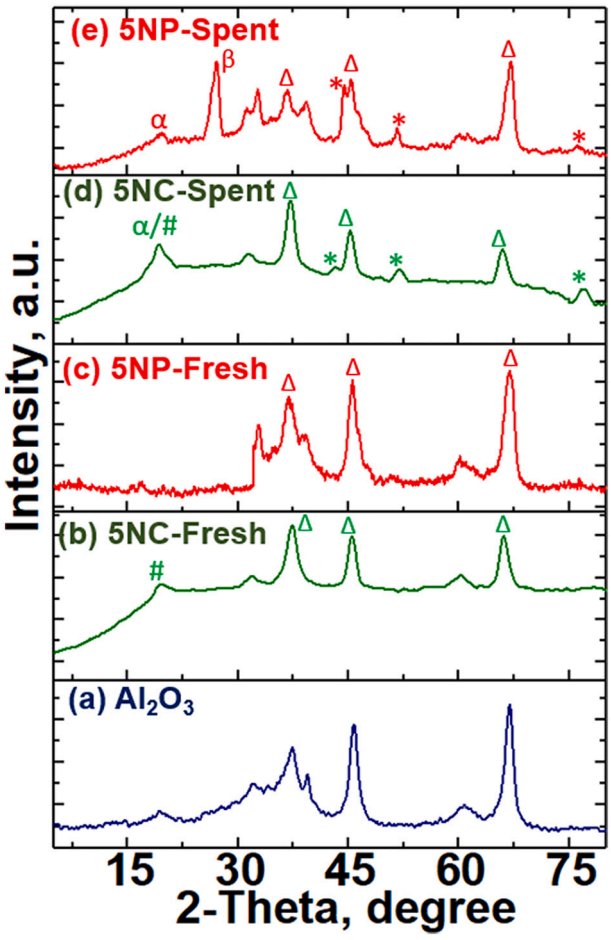

Fig. 2. X-ray diffraction patterns of the calcined catalysts, (a) γ-Al_2O_3, (b) 5NC calcined, (c) 5NP calcined, (d) 5NC spent and, (e) 5NP spent. Where symbols; * = metallic Ni^0, α = amorphous carbon, β = graphitic carbon, Δ = alumina, # = $NiAl_2O_4$.

studied using the analysis techniques of High-resolution transmission microscopy (HRTEM), corresponding Fast Fourier transform (FFT) of selected grains in the sample, and Rings in Selected Area Diffraction (SAED) patterns of the selected area. Representative HRTEM, FFT and EDS images of the 5NC catalyst are shown in Fig. 3. The comparatively darker contrast was sufficient for distinguishing nickel oxide particles from Al_2O_3 as support. As can be seen, for the 5NC catalyst, Ni nanoparticles were homogeneously dispersed over the Al_2O_3 support. Fig. 3b shows FFT of the HRTEM and experimental values from FFT. The experimental lattice spacing for the possible expected structure (Ni, NiO, $NiAl_2O_4$ and Al_2O_3) better matched with the theoretical $NiAl_2O_4$ cubic Fd3m phase [36]. As shown in Fig. 3c, the SAED patterns confirmed the presence of polycrystals. Moreover, SAED analysis results were also consistent with FFT pattern results and the observed phase matched with the $NiAl_2O_4$ phase. It is worth to mention that presence of metallic nickel or NiO species were not observed. As can be seen in Fig. 4, for the 5NP catalyst distribution of nickel particles was also uniform. However, the nickel particle size was comparatively bigger with a broader range of size distribution. The experimental lattice spacing values from the FFT of the HRTEM and SAED analysis of the 5NP catalyst matched with the theoretical rocksalt NiO Fm3m phase [36]. The average metal particle sizes for the 5NC and 5NP catalysts was found to be 6.3 ± 0.9nm and 16.5 ± 5.5, respectively.

3.2.2. *X-ray photoelectron spectroscopic analysis*

The XPS of the $Ni2p_{2/3}$ of the calcined catalysts are exhibited in Fig. 5. As can be seen, clear differences in XPS patterns of both catalysts was recorded. The position and shape of $Ni2p_{2/3}$ of both the samples were different indicating presence of different valence of the nickel species. As shown in Fig. 5a, the binding energy and shape of $Ni2p_{3/2}$ core level region of the 5NP was typical to occurrence of NiO. Suggesting that nickel was mainly present in the form of loosely interacting nickel oxide species. The XPS core-level Ni2p3/2 spectrum of the 5NC catalyst was much broader and at higher binding energy values indicating a heterogeneity in the chemical environment of nickel. As exhibited in Fig. 5b, the $Ni2p_{3/2}$ spectrum of the 5NC catalyst was deconvoluted into three species: the first peak at a binding energy of 853.2 eV was assigned to free and/or loosely interacting nickel oxide species, the second peak located at 854.4 eV was attributed to the presence of Ni^{2+} species experiencing stronger metal-support interactions. The third peak appearing at high binding energy of 856.1 eV has been reported to be characteristic of $NiAl_2O_4$ nanocrystallites [27,37]. It was worth noticing that the XPS of the catalyst 5NP did not show peaks corresponding to highly ionized Ni^{2+} species. Therefore, it is worth to conclude from the XPS analysis results, that for the calcined 5NC catalyst, nickel was present in the form of associated nickel oxide and highly induced $NiAl_2O_4$. By contrast, for the 5NP catalyst, a large amount of surface nickel was in the form of weekly interacting NiO species.

3.2.3. *Reducibility of the catalysts*

The sequential reduction following by oxidation and second reduction of the catalysts was studied by cyclic TPR-TPO and the results are displayed in Fig. 6 and Fig. 7. As can be seen in Fig. 6a, the TPR1 thermogram of the 5NP catalyst displayed spectrum consisted of four reduction peaks. The first broader reduction peak with maxima at 370 °C was attributed to the loosely associated NiO_x species to metallic Ni^o. The reduction peaks with maxima at 557 °C and 674 °C, respectively can be attributed to the nickel oxide species that either experience a strong metal interaction with support or have smaller particle size with better dispersion. The high reduction centered at 830 °C was assigned to the reduction of the nickel aluminate phases. As shown in Fig. 6b, the

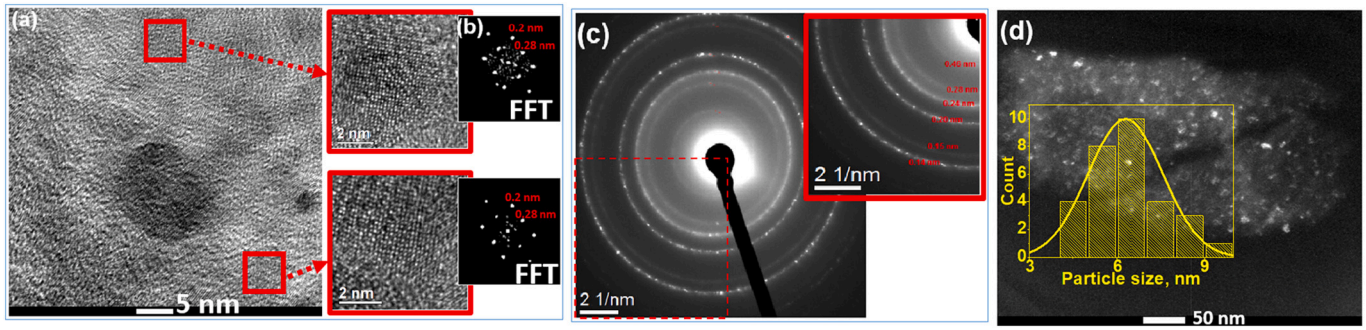

Fig. 3. (a) HRTEM, (b) Corresponding Fast Fourier Transform (FFT) of some grains in the sample, (c) Rings in Selected Area Diffraction (SAED) patterns of the selected area, and (d) metal particle size distribution of the as calcined 5NC catalyst.

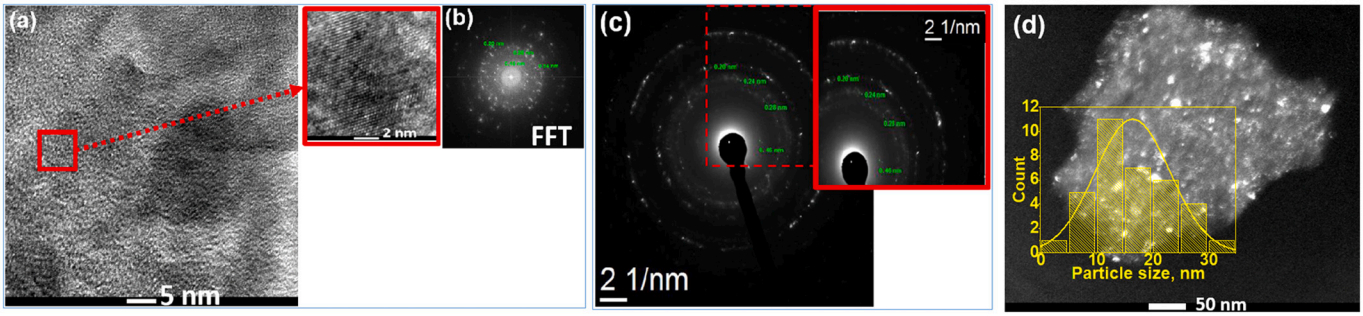

Fig. 4. (a) HRTEM, (b) Corresponding Fast Fourier Transform (FFT) of some grains in the sample, (c) Rings in Selected Area Diffraction (SAED) patterns of the selected area, and (d) metal particle size distribution of the as calcined 5NP catalyst.

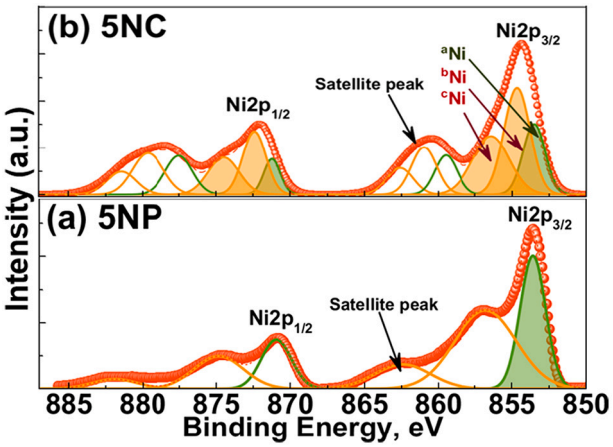

Fig. 5. Representative XPS Ni2p core-level spectra of the catalysts (a) 5NP, and (b) 5NC. Where, ^{a}Ni = loosely attached nickel species, ^{b}Ni = strongly associated nickel species, and ^{c}Ni = induced nickel species.

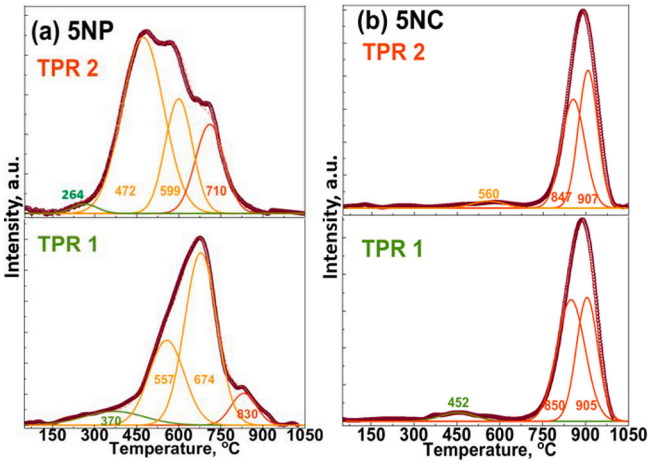

Fig. 6. Hydrogen temperature programmed (H_2-TPR) thermograms of the calcined catalyst samples (a) 5NP and (b) 5NC. Where TPR1 = First reduction profile of the calcined samples and TPR2 = second reduction profile after TPO.

TPR1 of the 5NC catalyst exhibited a remarkably different reduction behavior than the 5NP catalyst. From the H_2-TPR results, one can notice that for the 5NC catalyst the lower temperature reduction peaks are tiny whereas the high temperature reduction peaks are comparatively much larger than that of the 5NP catalyst. The TPR1 thermogram of the 5NC catalyst consisted of two peaks, which were deconvoluted into various peaks. The first low temperature peak appeared in the in the

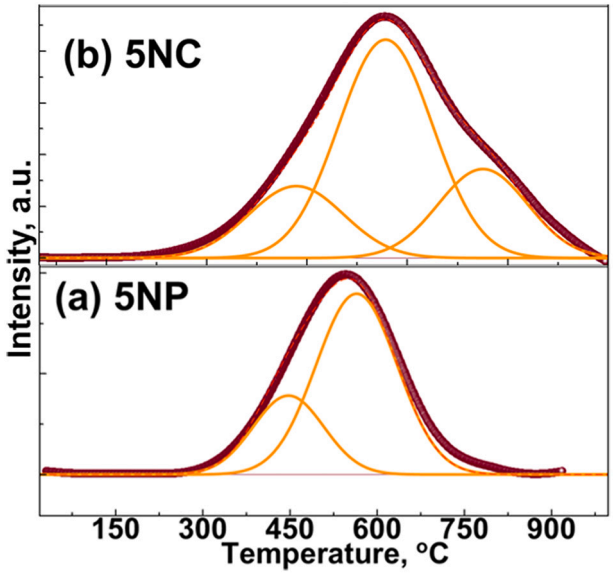

Fig. 7. Intermittent temperature programmed oxidation profiles (TPO) of the catalysts after TPR1 (a) 5NP and (b) 5NC.

temperature range between 320 °C to 600 °C (with maxima at 452 °C). This peak originated from reduction of the weakly interacting NiO_x species. The high temperature reduction peak deconvoluted into two peaks and with maxima at 850 °C and 905 °C, respectively. As reported in previous reports, these peaks were assigned to the reduction of nickel aluminate nanocrystallites [28,38,39]. Furthermore, the TPR1 results were also used for quantitative content of the NiO species. For the 5NC catalyst prepared by SCS method, 98% of the nickel species were in the form on $NiAl_2O_4$, whereas the case for the 5NP catalyst 90% was free NiO species loosely interacting with the support and only 8% of the nickel species were in the form of nickel aluminate. There results were consistent with the findings from the results of the XPS analysis, where larger amounts of induced Ni species were recorded suggesting an increased interaction for the sample synthesized by the SCS method. As can be seen in Fig. 7, the subsequent TPO curves followed by TPR1 of both the catalysts were characterized by a complex and broad oxidation peak in the range between 300 °C to 750 °C for the 5NP catalyst and whereas for the 5NC catalyst TPO curve was in the range between 300 °C to 900 °C. It is worth to mention that the 5NP catalyst appeared oxidize more easily than the 5NC catalyst. The sequential TPR2 confirmed the stability of the nickel phases of the 5NC catalyst. As shown in Fig. 6b, the thermogram of TPR2 displayed reduction patterns similar to observed in the TPR1. A similar behavior has been previously reported where the Ni-based catalyst maintained a consistent reduction profile during several reduction and oxidation cycles [40]. It is reasonable to hypothesize that

for the 5NC catalyst nickel species did not segregate and restored the species present in the calcined samples namely $NiAl_2O_4$. It is worth noticing that the synthesis methodology played a key role in nature and as well as stability of nickel species. The TPR2 profile of the 5NP catalyst revealed a completely different behavior than the TPR1. Conversely, main peak in the TPR2 shifted to low temperature. As revealed by the results of XPS analysis, the 5NP catalyst Ni was mainly found in the form of NiO weakly interacting with the support. Thus, it is reasonable to conclude that NiO resulted in an agglomeration in TPR1 cycle and consequently reduction temperature was shifted to lower degree in TPR2. Indeed TPR affirmed the findings from TEM and XPS analysis that the 5NC catalyst prepared by SCS method resulted in the formation of $NiAl_2O_4$ nanocrystallites phases in which the Ni^{2+} ions were possibly induced into the lattice of Al_2O_3 support.

3.3. Activity of the catalysts during steam reformation of methane

Methane conversion rates for both the catalysts were measured at steady state at a reaction temperature of 700 °C and the results are summarized in Table 1. The 5NC catalyst demonstrated exceptionally higher catalytic performance than the 5NP catalyst prepared by co-precipitation method. The rate of CH_4 decomposition over the 5NC catalyst was 527.5 μmol/gNi.s and was around five times higher than the rates over the 5NP catalyst (103.24 μmol/gNi.s). As will be discussed in later section, this difference in the catalytic activity was attributed to differences in various physicochemical properties of both catalysts.

The light-off break through curves demonstrated the effects of the preparative methodology as well as the effects of chemical structure on methane conversion, product distribution and stability as a function of reaction temperature. The results are displayed in Fig. 8. As demonstrated both the 5NC and 5NP catalysts displayed a different light off behavior for methane conversion. In the case of the 5NP catalyst, the light-off of CH_4 conversion was 600 °C and no conversion was observed at a reaction temperature below 600 °C. As can be seen, after the light-off at 600 °C, the conversion of methane started increasing with increase in operating temperature and finally a maximum of around 97.68% was achieved at around 900 °C. It is important to highlight that with the 5NP catalyst a complete methane decomposition never reached. As shown in Fig. 8, the light-off conversion profiles over the 5NC catalyst evidenced superior catalytic performance than that of the 5NP catalyst. The novel 5NC catalyst exhibited exceptionally high activity for methane reformation even below 600 °C. The start of the light-off over the 5NC catalyst was observed at 350 °C compared to 600 °C recorded for the 5NP catalyst. Methane conversion over the 5NC catalyst also increased with increase in reaction temperature and a full conversion was observed at around 700 °C. Increase in methane conversion with increase in operating temperature is in accordance with the reported literature [41–43]. As discussed earlier, steam reformation reaction is endothermic in nature and understandably, increase in operating temperature favored methane conversion. It is important to highlight that under similar reaction conditions methane conversion was 48% less over the 5NP catalyst. Increase in temperature resulted in an increase in CO and H_2 selectivities whereas CO_2 selectivity decreased. As can be seen in Fig. 8e, for both catalysts a decrease in the H_2/CO ratios with increase in the reaction temperature up to 650 °C was observed. Whereas, in the temperature range between 700 °C to 900 °C the H_2/CO ratio did not change. The effects of temperature on the ratio of H_2/CO seemed to be more pronounced for the 5NC catalyst. Moreover, the catalytic performance data results also revealed that the average H_2/CO value for the 5NC catalyst was higher than that of the 5NP catalyst. Similar trends have been reported in the literature and this behavior has been attributed to simultaneous existence of water gas shift reaction (WGSR) and the reverse water gas shift reaction (RWGSR) [5,18,44]. Indeed, for the 5NC catalyst at an operating temperature range below 650 °C, WGSR contributed to higher hydrogen production and thus resulted in hydrogen-enriched synthesis gas with higher H_2/CO ratios. Since, RWGSR is endothermic in nature and elevated temperature > 700 °C therefore favored the production of more CO and decreasing the overall H_2/CO ratios.

Table 1
Methane decomposition rates and physical properties of the catalysts.

Sample	Ni [wt%][ab]	Metal particle size, TEM	Reaction rate, [μmol/gNi.s][c]
5NC	6.53y	6.3 ± 0.99	527.47
5NP	15.21	16.5 ± 5.52	103.24

[a] XPS analysis.
[b] N_2-Adsorption & desorption by BET.
[c] Measured at stabilized CH_4 conversion at 700 °C.

The exceptionally high catalytic performance of the 5NC catalyst for the steam reformation of methane can be attributed to various unique chemical and physical properties of the 5NC catalyst. The analysis results of HRTEM analysis revealed that large percentage of nickel species over the 5NC catalyst were smaller with uniform distribution and mainly existed in the form of associated $NiAl_2O_4$ species. The TPR analysis also revealed that nickel species mainly existed in the form strongly associated and/or induced $NiAl_2O_4$ nanocrystallites spinels. By contrast, the 5NP catalyst mainly consisted of bulk NiO species with a small percentage of induced and/or strongly associated species. The metal oxide particle size of the 5NP catalyst was also comparatively larger.

3.4. Catalytic stability

A stability test for steam reformation of methane for both the catalysts was performed at a reaction temperature of 700 °C and steam to methane ratio of unity for around 200 h. The stability test focused on comparison between the extent of activity in terms of decrease in methane conversion and deactivation. Fig. 9 represents the change in activity on the 5NP and 5NC catalysts under similar reaction conditions. As can be seen, for the 5NC catalyst there was no observable change and/or decrease in percentage conversion of methane during the 200 h test. By contrast, decrease in CH_4 conversion with T.O·S. was evident over the 5NP catalyst. The 5NP catalyst experienced continuous decrease in methane conversion and catastrophic deactivation began at around 52 h online. The 5NP catalyst lost its activity and structure and the reactor was plugged at around 75 h T.O.S. presumably due to the considerable amount of coke deposition.

3.4.1. Characterization of the spent catalysts

As discussed in earlier deposition of carbon on the Ni-based catalysts surface during SRM has a significant contribution to the catalyst deactivation. Indeed, the mechanism of surface coke deposition during SRM is well described in the reported literature [5,45–48]. Thus, the TPO analysis results for both the 5NC and 5NP catalysts passivated in inert environment followed steam reformation reaction at 700 °C for T.O.S of 200 h are presented in Fig. 10. Carbon dioxide was the only gas produced and other gases were not detected. Both the catalysts showed different patterns of CO_2 evolution upon heating. As can be seen, TPO thermogram of the 5NP catalyst revealed the presence of one broader peak in the temperature range between 450 °C to 900 °C which was deconvoluted into two distinct peaks with maxima at 600 °C and 745 °C, respectively. The first peak denoted as C2 was attributed to the presence of amorphous carbon whereas the second peak denoted at C3 was due the oxidation of filamenreous coke deposited on the surface. The relative percentages (C2/C2 + C3) of C2 and C3 was 21.85% and 78.14%, respectively indicating that on the surface of the 5NP catalyst carbon was mainly deposited in the form of filamentous carbon. Moreover, it is worth to mention that at a temperature < 400 °C no CO_2 peak was observed. Contrary to 5NP, the 5NC catalyst exhibited of three distinct CO_2 evolution peaks indicating the presence of three surface carbon species. The first peak with maxima at 358 °C (denoted as C1) was assigned to the oxidation of reaction intermediates and/or active carbon

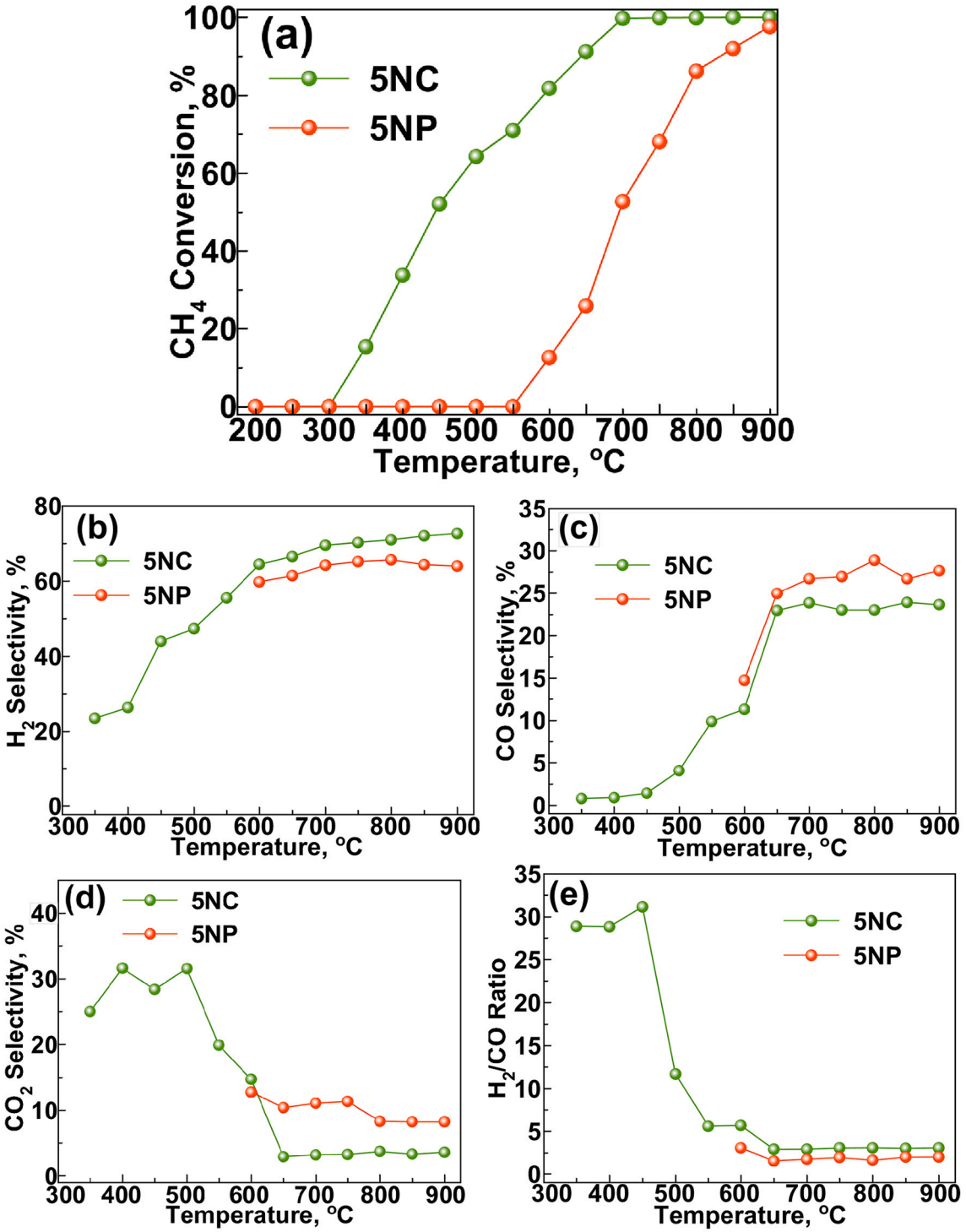

Fig. 8. Light-off curves demonstrating the effects of temperature on (a) CH_4 conversion, (b) H_2 selectivity, (c) CO selectivity, (d) CO_2 selectivity and (e) H_2/CO ratios. Reaction conditions were; GHSV = 9000 h^{-1}, CH_4/H_2O ratio = 3, and at atmospheric pressure.

species. Similarly, the second peak (C2) in the temperature range between 300 °C to 500 °C was attributed to the presence of graphitic and/or amorphous carbon. The third peak (denoted as C3) was with comparatively smaller intensity appeared in the temperature range between 590 °C to 750 °C originated due to oxidation of the filamentous carbon. It has been reported that filamentous carbon oxidizes at high temperatures [49–51]. The relative population (C1/C1 + C2 + C3) of C1, C2 and C3 was 56.9%, 22.4% and 20.62%, respectively. It must be pointed out that for the 5NC, catalyst witnessed a significant reduction in the formation of filamentous carbon and carbon was mainly present in the form of filamentous and reactive carbon.

Moreover, in order to study textural stability of the catalysts after longer run of T.O.S. for steam reformation reaction, the spent catalysts were also analyzed for N2 adsorption and desorption and the results are presented in Table 2. Indeed, the BET analysis results of the spent catalysts confronted the finding from TPO analysis. As summarized in Table 2, the spent 5NP catalyst had underwent change in textural properties. Compared with the freshly calcined sample, there was an

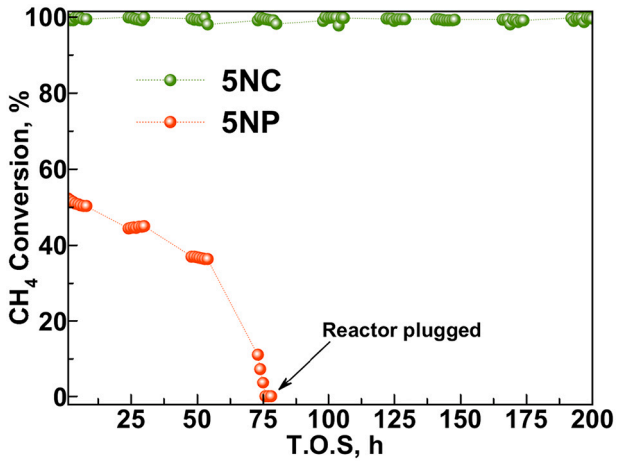

Fig. 9. Catalytic performance in terms of methane conversion in time on stream over the 5NC and 5NP catalysts. Reaction conditions were; $T = 750$ °C, $CH_4/H_2O = 1$, GHSV = 9000 h^{-1}.

increase in pore size, pore volume and surface area suggesting porous coke deposition on the catalyst surface. Contrary to 5NP catalyst, the 5NC catalyst recorded a decrease in surface area by around 5%, marginal decrease in pore volume and pore size. Decrease in surface area of the 5NC catalyst can be attributed to the deposition of amorphous carbon. In addition, the results indicated also that the 5NC catalyst was physically stable.

XRD patterns of the spent catalysts after stability test are shown in Fig. 2. The XRD analysis results of the spent catalysts affirmed the findings from the TPO analysis results. As can be seen, both catalysts revealed presence of new diffraction lines. The diffraction lines at 2θ values of 44.05°, 51.8°, and 76.4° degree were attributed to the presence of metallic nickel [52]. For the 5NP catalyst, the new peaks at 2θ of ~20° and 26.8° can be attributed to the presence of amorphous carbon and graphitic carbon respectively. The diffraction line corresponding to graphitic carbon was comparatively more intense. It is worth to mention that the graphitic carbon related peak was observed for the 5NC catalyst affirming that carbon deposited was amorphous in nature.

These results strongly indicate that the 5NC catalyst was resilient to coke deposition and did not experience deactivation during the tested period of around two hundred hours. This behavior can be attributed to the smaller particle size, presence of surface defects, oxygen vacancies and induced metal oxide phases in the form of $NiAl_2O_4$ crystallites. Presence of these properties of the 5NC catalyst presumably favored the removal of surface carbon and thus the carbon mainly deposited in the form of amorphous species making the catalyst coke resilient. On the other hand, the high amount of coke deposition that oxidized at higher temperature was responsible for deactivation of the 5NP catalyst. Indeed, the deposition of more carbon on the 5NP catalyst can be attributed to lesser oxygen mobility due to presence of unassociated NiO species with comparatively larger sizes as revealed by the analysis techniques. Previous reports have also suggested deactivation of Ni-based catalysts due to presence of larger particle size and absence of strong metal support interactions (SMSI) [53–55]. Moreover, the reported literature suggest that presence of stronger metal support interaction and/or presence of induced metal phases are crucial for stability of the Ni-based catalysts for reformation reaction [56–58].

4. Conclusions

The 5NC catalyst prepared by the SCS method displayed different catalytic performances than the 5NP catalyst in the steam reformation reaction of methane. The light off over the 5NC catalyst appeared at 350 °C and a complete methane conversion was attained at an operating temperature of 700 °C. The 5NP catalyst prepared by co-precipitation method was inactive below <600 °C and complete methane conversion was not achieved. The yields of H_2 and CO over the 5NC catalyst were also higher than the 5NP. The 5NC catalyst exhibited a stable activity for a period of 200 h by contrast the 5NP catalyst experienced decrease in methane conversion and catastrophic deactivation occurred at T.O.S of 70 h. The difference in catalytic behavior during steam reformation reaction was attributed to the difference in physicochemical properties as revealed by the analysis results of XRD, TEM, XPS and TPR. The high catalytic activity with superior stability of the 5NC catalyst was mainly due to the presence of well-dispersed, small metal oxide nanoparticles experiencing strong metal support interactions and due to the presence of $NiAl_2O_4$ nanocrystallite structures. By contrast, the 5NP mainly consisted of loosely attached NiO species with comparatively larger metal oxide particles that responsible for deposition of filamentous carbon on the catalyst surface resulting in serious deactivation.

CRediT authorship contribution statement

Sardar Ali: Conceptualization, Methodology, Data curation, Writing – original draft, Investigation. **Ahmed Gamal:** Data curation, Formal

Table 2
Results of N_2-adsorption and desorption analysis.

Sample	S.A. BET (m^2/g)		Pore volume (cm^3/g), BJH		Mean pore diameter (Å), BJH	
5NP	Fresh	Used	Fresh	Used	Fresh	Used
	53.6	61.5	0.14	0.15	46.6	47.3
5NC	98.9	93.9	0.21	0.16	30.8	28.7

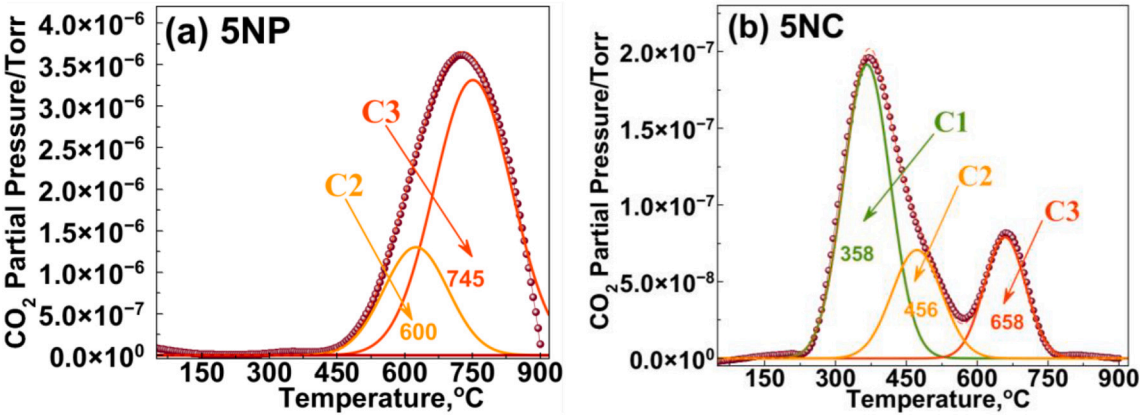

Fig. 10. Temperature programmed oxidation (TPO) profiles of the used catalysts after 200 h of reaction for steam methane reforming, (a) 5NP, and (b) 5NC.

analysis. **Mahmoud M. Khader:** Supervision, Writing – review & editing.

Declaration of Competing Interest

The authors have no competing interests to declare.

Data availability

Data will be made available on request.

Acknowledgements

This paper was made possible by a NPRP Grant #6-290-1-059 From the Qatar National Research Fund (a member of Qatar Foundation). The statements made herein are solely the responsibility of the authors.

References

[1] A. Kaddouri, B.J.C.C. Béguin, Methane steam reforming in the absence and presence of H2S over Ce0. 8Pr0. 2O2− δ, Ce0. 85Sm0. 15O2− δ and Ce0. 9Gd0. 1O2− δ SOFCs anode materials 46 (2014) 22–27.
[2] X. Guo, Y. Sun, Y. Yu, X. Zhu, C.-J.J.C.C. Liu, Carbon formation and steam reforming of methane on silica supported nickel catalysts 19 (2012) 61–65.
[3] L. Zhou, Y. Guo, Q. Zhang, M. Yagi, H. Li, J. Chen, M. Sakurai, H.J.C.C. Kameyama, Self-activation and self-regenerative activity of trace Ru-doped plate-type anodic alumina supported nickel catalysts in steam reforming of methane 10 (2008) 325–329.
[4] U. Rodemerck, M. Schneider, D.J.C.C. Linke, Improved stability of Ni/SiO2 catalysts in CO2 and steam reforming of methane by preparation via a polymer-assisted route 102 (2017) 98–102.
[5] E. Meloni, M. Martino, V.J.C. Palma, A short review on Ni based catalysts and related engineering issues for methane steam reforming 10 (2020) 352.
[6] P. Mierczynski, M. Mosinska, N. Stepinska, K. Chalupka, M. Nowosielska, W. Maniukiewicz, J. Rogowski, N. Goswami, K. Vasilev, M.I.J.C.T. Szynkowska, Effect of the support composition on catalytic and physicochemical properties of Ni catalysts in oxy-steam reforming of methane 364 (2021) 46–60.
[7] L. Chen, J. Zhang, X.J.C.C. Liang, Reducing gas atmosphere (H2, CO) assisted formation of Fe-Ce-Ox composite oxides with enhanced catalytic activity for water-gas shift reaction 138 (2020), 105849.
[8] J. Niu, Y. Wang, Y. Qi, A.H. Dam, H. Wang, Y.-A. Zhu, A. Holmen, J. Ran, D.J. F. Chen, New mechanism insights into methane steam reforming on Pt/Ni from DFT and experimental kinetic study 266 (2020), 117143.
[9] W.N. Manan, W.N.R. Wan Isahak, Z.J.C. Yaakob, CeO2-based heterogeneous catalysts in dry reforming methane and steam reforming methane: A short review 12 (2022) 452.
[10] H. Zhang, Z. Sun, Y.H.J.R. Hu, S.E. Reviews, Steam reforming of methane: Current states of catalyst design and process upgrading 149 (2021), 111330.
[11] P. Summa, B. Samojeden, M.J.P.J.O.C.T. Motak, Dry and steam reforming of methane. Comparison and analysis of recently investigated catalytic materials. A short review 21 (2019).
[12] Y.S. Park, M. Kang, P. Byeon, S.-Y. Chung, T. Nakayama, T. Ko, H.J.J.O.P. S. Hwang, Fabrication of a regenerable Ni supported NiO-MgO catalyst for methane steam reforming by exsolution 397 (2018) 318–324.
[13] A. Etminan, S.J.F. Sadrnezhaad, A two step Microwave-assisted coke resistant mesoporous Ni-Co catalyst for methane steam reforming 317 (2022), 122411.
[14] A. Salcedo, P.G. Lustemberg, N. Rui, R.M. Palomino, Z. Liu, S. Nemsak, S. D. Senanayake, J.A. Rodriguez, M.V. Ganduglia-Pirovano, B.J.A.C. Irigoyen, Reaction pathway for coke-free methane steam reforming on a Ni/CeO2 catalyst: active sites and the role of metal–support interactions 11 (2021) 8327–8337.
[15] M. Wang, X. Tan, J. Motuzas, J. Li, S.J.J.O.M.S. Liu, Hydrogen production by methane steam reforming using metallic nickel hollow fiber membranes 620 (2021), 118909.
[16] J. Zhou, J. Zhao, J. Zhang, T. Zhang, M. Ye, Z.J.C.J.O.C. Liu, Regeneration of catalysts deactivated by coke deposition: A review 41 (2020) 1048–1061.
[17] A. Fasolini, S. Ruggieri, C. Femoni, F.J.C. Basile, Highly active catalysts based on the Rh4 (CO) 12 cluster supported on Ce0. 5Zr0. 5 and Zr oxides for low-temperature methane steam reforming 9 (2019) 800.
[18] H. Wang, M. Liu, H. Kong, Y.J.A.T.E. Hao, Thermodynamic analysis on mid/low temperature solar methane steam reforming with hydrogen permeation membrane reactors 152 (2019) 925–936.
[19] N. Panchan, W. Donphai, J. Junsomboon, C. Niamnuy, M.J.A.O. Chareonpanich, Influence of the calcination technique of silica on the properties and performance of Ni/SiO2 catalysts for synthesis of hydrogen via methane cracking reaction 4 (2019) 18076–18086.
[20] L. Azancot, L.F. Bobadilla, M.A. Centeno, J.A.J.J.O.C.U. Odriozola, Effect of potassium loading on basic properties of Ni/MgAl2O4 catalyst for CO2 reforming of methane 52 (2021), 101681.
[21] M. Torimoto, S. Ogo, Y. Hisai, N. Nakano, A. Takahashi, Q. Ma, J.G. Seo, H. Tsuneki, T. Norby, Y.J.R.A. Sekine, Support effects on catalysis of low temperature methane steam reforming 10 (2020) 26418–26424.
[22] A. Kambolis, H. Matralis, A. Trovarelli, C.J.A.C.A.G. Papadopoulou, Ni/CeO2-ZrO2 catalysts for the dry reforming of methane 377 (2010) 16–26.
[23] M. Bradford, M.J.C.R. Vannice, CO2 reforming of CH4 41 (1999) 1–42.
[24] T. Huang, W. Huang, J. Huang, P.J.F.P.T. Ji, Methane reforming reaction with carbon dioxide over SBA-15 supported Ni–Mo bimetallic catalysts 92 (2011) 1868–1875.
[25] N. Salhi, A. Boulahouache, C. Petit, A. Kiennemann, C.J.I.J.O.H.E. Rabia, Steam reforming of methane to syngas over NiAl2O4 spinel catalysts 36 (2011) 11433–11439.
[26] D. Li, Y. Li, X. Liu, Y. Guo, C.-W. Pao, J.-L. Chen, Y. Hu, Y.J.A.C. Wang, NiAl2O4 spinel supported Pt catalyst: high performance and origin in aqueous-phase reforming of methanol 9 (2019) 9671–9682.
[27] M.H. Aghaali, S.J.I.J.O.H.E. Firoozi, Enhancing the catalytic performance of Co substituted NiAl2O4 spinel by ultrasonic spray pyrolysis method for steam and dry reforming of methane 46 (2021) 357–373.
[28] X. Fang, R. Zhang, Y. Wang, M. Yang, Y. Guo, M. Wang, J. Zhang, J. Xu, X. Xu, Plasma assisted preparation of highly active NiAl2O4 catalysts for propane steam reforming 46 (2021) 24931–24941.
[29] M.S. Yancheshmeh, O.A. Sahraei, M. Aissaoui, M.C.J.A.C.B.E. Iliuta, A novel synthesis of NiAl2O4 spinel from a Ni-Al mixed-metal alkoxide as a highly efficient catalyst for hydrogen production by glycerol steam reforming 265 (2020), 118535.
[30] C. Venkataramana, S.M. Botsa, P. Shyamala, R.J.C. Muralikrishna, Photocatalytic degradation of polyethylene plastics by NiAl2O4 spinels-synthesis and characterization 265 (2021), 129021.
[31] S. Ali, M.M. Khader, M.J. Almarri, A.G.J.C.T. Abdelmoneim, Ni-based nano-catalysts for the dry reforming of methane 343 (2020) 26–37.
[32] I.E. Achouri, N. Abatzoglou, C. Fauteux-Lefebvre, N.J.C.T. Braidy, Diesel steam reforming: Comparison of two nickel aluminate catalysts prepared by wet-impregnation and co-precipitation 207 (2013) 13–20.
[33] J. Li, R. Zhang, Y. Liu, T. Sun, J. Jia, M.J.C.C. Guo, Enhanced catalytic activity of toluene oxidation over in-situ prepared Mn3O4-Fe2O3 with acid-etching treatment, (2022) 106581.
[34] W. Gou, X. Mo, C. Ren, H. Wang, W.J.C. Li, Formation of crystalline multimetallic layered double hydroxide precipitates during uptake of Co, Ni, and Zn onto γ-alumina: Evidence from EXAFS, XRD, and TEM 307 (2022), 136055.
[35] N. García-Gómez, J. Valecillos, A. Remiro, B. Valle, J. Bilbao, A.G.J.A.C.B. E. Gayubo, Effect of reaction conditions on the deactivation by coke of a NiAl2O4 spinel derived catalyst in the steam reforming of bio-oil 297 (2021), 120445.
[36] R. Downs, K. Bartelmehs, G. Gibbs, M.J.A.M. Boisen, Interactive software for calculating and displaying X-ray or neutron powder diffractometer patterns of crystalline materials 78 (1993) 1104–1107.
[37] S. Zhang, M. Ying, J. Yu, W. Zhan, L. Wang, Y. Guo, Y.J.A.C.B.E. Guo, NixAl1O2-δ mesoporous catalysts for dry reforming of methane: The special role of NiAl2O4 spinel phase and its reaction mechanism 291 (2021), 120074.
[38] S. Iglesias-Vázquez, J. Valecillos, A. Remiro, J. Bilbao, A.G.J.C. Gayubo, Stability of a NiAl2O4 derived catalyst in the ethanol steam reforming in reaction-regeneration cycles, Effect of Reduction Temperature 12 (2022) 550.
[39] B.C. Kwon, N.-K. Park, M. Kang, D. Kang, M.W. Seo, D. Lee, S.G. Jeon, CO2 hydrogenation activity of Ni-Mg-Al2O3 catalysts: Reaction behavior on NiAl2O4 and MgAl2O4 38 (2021) 1188–1196.
[40] D. Li, I. Atake, T. Shishido, Y. Oumi, T. Sano, K.J.J.O.C. Takehira, Self-regenerative activity of Ni/Mg (Al) O catalysts with trace Ru during daily start-up and shut-down operation of CH4 steam reforming 250 (2007) 299–312.
[41] M. Ambrosetti, D. Bonincontro, R. Balzarotti, A. Beretta, G. Groppi, E.J.C. T. Tronconi, H2 production by methane steam reforming over Rh/Al2O3 catalyst packed in Cu foams: A strategy for the kinetic investigation in concentrated conditions 387 (2022) 107–118.
[42] M.R. Almind, S.B. Vendelbo, M.F. Hansen, M.G. Vinum, C. Frandsen, P. M. Mortensen, J.S.J.C.T. Engbæk, Improving performance of induction-heated steam methane reforming 342 (2020) 13–20.
[43] A.H. Martínez, E. Lopez, L.E. Cadús, F.N.J.C.T. Agüero, Elucidation of the role of support in Rh/perovskite catalysts used in ethanol steam reforming reaction 372 (2021) 59–69.
[44] Q. Zhao, Y. Wang, Y. Wang, L. Li, W. Zeng, G. Li, C.J.I.J.O.H.E. Hu, Steam reforming of CH4 at low temperature on Ni/ZrO2 catalyst: Effect of H2O/CH4 ratio on carbon deposition 45 (2020) 14281–14292.
[45] S.M. Hashemnejad, M.J.C.J.O.C. Parvari, Deactivation and regeneration of nickel-based catalysts for steam-methane reforming 32 (2011) 273–279.
[46] J.R.J.C.T. Rostrup-Nielsen, Industrial relevance of coking 37 (1997) 225–232.
[47] S. Kameshima, K. Tamura, R. Mizukami, T. Yamazaki, T.J.P.P. Nozaki, Polymers, Parametric analysis of plasma-assisted pulsed dry methane reforming over Ni/Al2O3 catalyst 14 (2017) 1600096.
[48] H. Wu, V. La Parola, G. Pantaleo, F. Puleo, A.M. Venezia, L.F.J.C. Liotta, Ni-based catalysts for low temperature methane steam reforming: recent results on Ni-Au and comparison with other bi-metallic systems 3 (2013) 563–583.
[49] S. Ali, M.J. Al-Marri, A.G. Abdelmoneim, A. Kumar, M.M.J.I.J.O.H.E. Khader, Catalytic evaluation of nickel nanoparticles in methane steam reforming 41 (2016) 22876–22885.
[50] B. Han, F. Wang, L. Zhang, Y. Wang, W. Fan, L. Xu, H. Yu, Syngas production from methane steam reforming and dry reforming reactions over sintering-resistant Ni@SiO2 catalyst 46 (2020) 1735–1748.

[51] L.P. Profeti, E.A. Ticianelli, E.M.J.F. Assaf, Co/Al2O3 catalysts promoted with noble metals for production of hydrogen by methane steam reforming 87 (2008) 2076–2081.
[52] F. Zhang, Z. Liu, X. Chen, N. Rui, L.E. Betancourt, L. Lin, W. Xu, C.-j. Sun, A. M. Abeykoon, J.A.J.A.C. Rodriguez, Effects of Zr doping into ceria for the dry reforming of methane over Ni/CeZrO2 catalysts: in situ studies with XRD, XAFS, and AP-XPS 10, 2020, pp. 3274–3284.
[53] J.F. Gonçalves, M.M.J.C.L. Souza, Effect of doping niobia over Ni/Al2O3 catalysts for methane steam reforming 148 (2018) 1478–1489.
[54] D.L.J.C.T. Trimm, Coke formation and minimisation during steam reforming reactions 37 (1997) 233–238.
[55] L. Chen, Q. Huang, Y. Wang, H. Xiao, W. Liu, D. Zhang, T.J.I.J. Yang, Tailoring performance of Co–Pt/MgO–Al2O3 bimetallic aerogel catalyst for methane oxidative carbon dioxide reforming, Effect of Pt/Co ratio 44 (2019) 19878–19889.
[56] Z. Taherian, V.S. Gharahshiran, A. Khataee, Y.J.J.O.I. Orooji, E. Chemistry, Anti-coking freeze-dried NiMgAl catalysts for dry and steam reforming of methane 103 (2021) 187–194.
[57] Z. Rajabi, M. Martinelli, G.F. Upton, C.D. Watson, D.C. Cronauer, A.J. Kropf, G.J.C. T. Jacobs, Low temperature ethanol steam reforming: Selectivity control with lithium doping of Pt/m-ZrO2 402 (2022) 335–349.
[58] Z. Rajabi, L. Jones, M. Martinelli, D. Qian, D.C. Cronauer, A.J. Kropf, C.D. Watson, G.J.C. Jacobs, Influence of Cs Promoter on Ethanol Steam-Reforming Selectivity of Pt/m-ZrO2 Catalysts at Low Temperature 11, 2021, p. 1104.